

Medium-energy microprobe station at the SXRMB of the CLS

Qunfeng Xiao,^a Aimee MacLennan,^a Yongfeng Hu,^{a*} Mark Hackett,^b
Peter Leinweber^c and Tsun-Kong Sham^d

^aCanadian Light Source, 44 Innovation Boulevard, Saskatoon, SK, Canada S7N 2V3, ^bDepartment of Geological Sciences, University of Saskatchewan, Saskatoon, SK, Canada S7N 5E2, ^cSoil Science, Faculty for Agricultural and Environmental Sciences, University of Rostock, Justus-von-Liebig Weg 6, 18051 Rostock, Germany, and ^dDepartment of Chemistry, The University of Western Ontario, 1151 Richmond Street, London, ONT, Canada N6A 5B7.

*Correspondence e-mail: yongfeng.hu@lightsource.ca

Received 11 August 2016

Accepted 4 November 2016

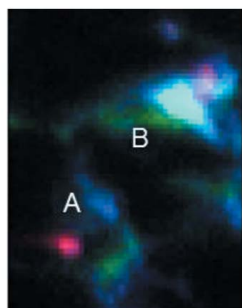
Edited by G. E. Ice, Oak Ridge National Laboratory, USA

Keywords: medium-energy beamline; micro-XAFS; micro-XRF.

Micro-XAFS and chemical imaging techniques have been widely applied for studies of heterogeneously distributed systems, mostly in hard X-ray (>5 keV) or in soft X-ray (<1.5 keV) energies. The microprobe endstation of the SXRMB (soft X-ray microcharacterization beamline) at the Canadian Light Source is optimized at the medium energy (1.7–5 keV), and it has been recently commissioned and is available for general users. The technical design and the performance (energy range, beam size and flux) of the SXRMB microprobe are presented. Examples in chemical imaging and micro-XAFS in the medium energy for important elements such as P, S and Ca for soil and biological samples are highlighted.

1. Introduction

Chemical analysis of materials at the microscopic scale (1–100 μm) is often required for many fundamental studies and industrial applications. Synchrotron-based X-ray microanalysis techniques, including microfluorescence, microspectroscopy and microdiffraction, are widely applied to studies in environmental, heritage, medical and material sciences (West *et al.*, 2015; Chadwick *et al.*, 2012). Most of these applications have been carried out using hard X-ray beamlines with a low end of photon energy around 2–3 keV; such as 13 ID at APS (Newville *et al.*, 1999), 20 ID at APS (Heald *et al.*, 2007), ID22 of ESRF (Martínez-Criado *et al.*, 2012), 10.3.2 at ALS (Marcus *et al.*, 2004), I18 at DLS (Mosselmann *et al.*, 2009), BL-15A1 at PF (Igarashi *et al.*, 2013) and several beamlines at SSRL (<http://www-ssrl.slac.stanford.edu/content/science/ssrl-imaging-group>). More recently, soft X-ray microscopy has been realised using STXM [scanning transmission X-ray microscopy; see Hitchcock (2015) for a summary of facilities, techniques and applications]. STXM typically covers the energy range 20–2000 eV with high spatial resolution (tens of nanometres). Microprobe capabilities in the soft X-ray range (50–1000 eV) using Kirkpatrick–Baez (KB) mirrors are also being implemented at the VLS-PGM and SGM beamlines of the CLS (T. K. Sham, private communication). However, with the exception of a few recent beamlines [LUCIA at SOLEIL (Vantelon *et al.*, 2016) and PHOENIX beamline at SLS], the medium-energy range (1.7–5 keV), sometimes referred to as tender X-rays, is not normally covered by the soft X-ray nor hard X-ray beamlines; the K-edge of some important elements, such as Si, S, P and Ca, lies in this energy region,



SXRMB (soft X-ray microcharacterization beamline) at the CLS is a bending-magnet-based beamline that utilizes InSb(111) and Si(111) crystals covering an energy range of 1.7–10 keV, with its main research focus in the medium energy (1.7–5 keV) (Hu *et al.*, 2010). Among the multiple endstations available at the SXRMB (vacuum XAFS, ambient XAFS, high-energy XPS and microprobe), the microprobe is the latest commissioned. This paper reports the design and performance of the microprobe endstation at the SXRMB, highlighting the application of microanalysis of soil and biological research in the medium-energy range.

2. Microprobe station

The SXRMB is designed with two focal spots, with the upstream one being the bulk spot, where the full beam (1.0 mrad × 0.5 mrad, H × V) was utilized. Two sets of crystals, InSb(111) and Si(111), were employed as the monochromator. These crystals were both water cooled and interchangeable under vacuum. The focusing of the first spot (XAFS station) is achieved by a vertical collimating mirror located at 14 m from the source, combined with a toroidal mirror (Hu *et al.*, 2010). The designed spot size is 260 μm × 230 μm, where multiple endstations (vacuum and ambient XAFS, and high-energy XPS, all portable) are fit into this space (Fig. 1). The micro-focusing of the microprobe station is achieved using KB mirrors, taking in 0.15 mrad × 0.15 mrad of the beam. Both KB mirrors are 200 mm long using Si substrates, with a carbon and Pt bi-layer reflective coating. Both mirrors work with a grazing-incidence angle of 0.45° (7.85 mrad). The first KB mirror deflects the beam vertically by 0.9° (15.7 mrad) and focuses the collimated beam generated by the first mirror of the beamline along the vertical direction. The second mirror deflects the beam sideways and focuses the collimated beam generated by the sagittal cylinder mirror 300 mm downstream horizontally. Both mirrors and

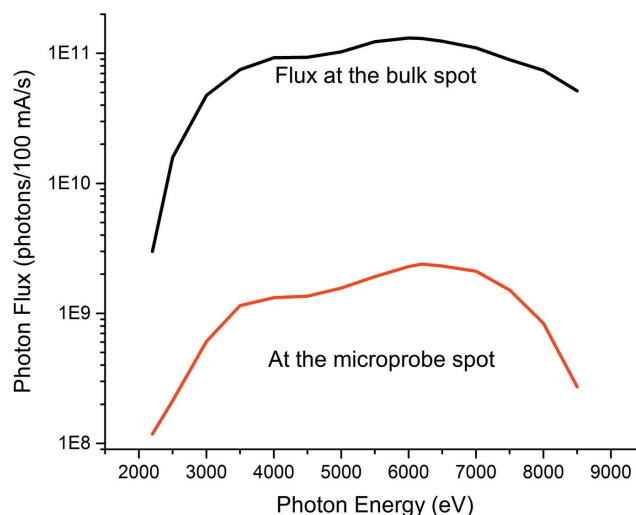


Figure 2
Photon fluxes of the SXRMB at the bulk XAFS and microprobe stations.

their motors (bending and adjustments) and controls are housed in a turbo-pumped chamber (Fig. 1). The sample stage is housed in a separate chamber downstream, equipped with a four-element Si(Li) drift detector, a CCD camera and a three-axis (*X*, *Y* and *Z*) sample stage. A micro-ion chamber is placed in between the KB mirror chamber and the sample chamber, for beam alignment and monitoring. Both chambers are fitted with a 25 μm Be window capable of withstanding the vacuum and up to approximately one atmosphere of inert gas, while having enough transmission over the lower energies covered by the beamline. The SXRMB is designed for fast switching between the (bulk and microprobe) endstations because the upstream XAFS station is normally under vacuum; the beam pipe and JJ X-ray slits inbetween the XAFS station and the KB chamber are also under vacuum.

SXRMB has a relatively large beam size because it uses a bending magnet source. The designed spot size at the microprobe spot is 10 μm × 10 μm, based on the geometrical demagnification factors (vertically, 14 m/0.6 m; horizontally, 18 m/0.3 m; for distances from the source see Fig. 1). Indeed, the measured spot size values are 11.0 μm (V) × 10.8 μm (H), using the knife-edge technique. The photon flux measured at the focal spot is around 10⁹ photons (100 mA)⁻¹ s⁻¹ (Fig. 2), about two orders of magnitude lower than at the corresponding bulk spot.

3. Scientific applications

The standard techniques available for microanalysis at the SXRMB are micro-XRF and micro-XAFS. With the use of the four-element SDD detector, one can map the elemental distribution and correlations of elements on a micro-

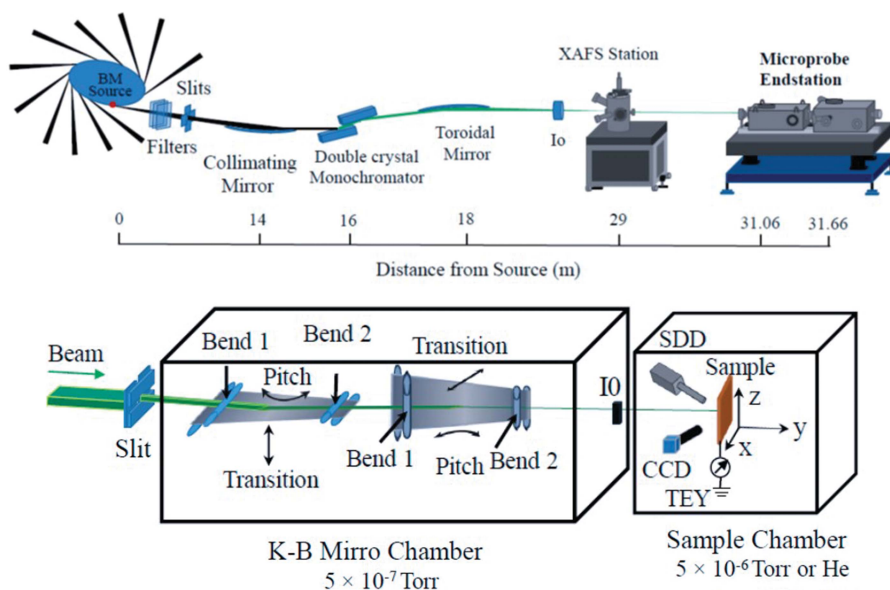


Figure 1
Sketch of the microprobe station at the SXRMB.

metre scale using micro-XRF. With the micro-XAFS scans, one can obtain the chemical speciation of elements, by recording XANES or EXAFS spectra of selected sample spots with grain sizes on the order of 10 μm . As the sample chamber is normally under vacuum, the SXRMB is also set up for mapping in total electron yield, which is more surface sensitive, complementary to the bulk-sensitive fluorescence yield. Additionally, the SXRMB is especially optimized for micro-XAFS of some difficult-to-cover elements, such as Si, P and S, because of its energy range. In the following, we will use three examples of diverse applications in the fields of soil science and biology to illustrate this capability.

3.1. Micro-XAFS study of a biological soil crust

Biological soil crusts are formed by communities of living organisms on the soil surface that glue inorganic particles as well as organic matter. They play important ecological roles, accounting for about 7% of global carbon fixation and 50% of global biological nitrogen fixation (Elbert *et al.*, 2012); and they could be a source of available nutrient phosphorus (P) in soil by concomitant dissolution of non-available P minerals (Belnap, 2011). However, the weathering mechanisms of the P-containing minerals in sediment and soil and the relationship between P sources and other biomaterials in the crusts are still unknown. In this study, a biogenic soil crust collected from an undisturbed coastal dune at Glowe, Island of Rügen, Germany, was selected for the elemental mapping and micro-XANES. A vertically cut section sample (3 mm \times 5 mm), where predominantly rounded quartz grains and the green algae could be visually distinguished, was mapped (Leinweber *et al.*, 2017).

Fig. 3 shows the XRF distributions of Si, P and Ca, together with the tri-colour map of P, S and Ca of a 500 μm \times 700 μm section, the individual map of S is not included as it has essentially the same distribution as that of P. It is observed that Si is enriched in a few hotspots that mostly do not coincide with enrichments of other elements. This is explained by the concentration of Si in quartz grains that are visible in the crust (Leinweber *et al.*, 2017). It is also clear that the Ca distribution is somewhat different from that of P and S, with a Ca hot spot (marked as A) containing very little P and S. The μ -XANES

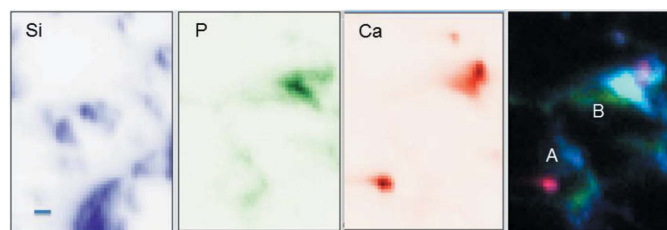


Figure 3

Elemental mapping of a biogenic soil crust, showing a relatively uniform distribution of Si, with a few hot spots with elevated concentrations of P and Ca. Three images are the individual elemental maps and the right-hand image is the tri-colour map of Ca (red)/P (green)/S (blue), with two hot spots (A and B) marked. Scale bar = 50 μm (individual map of S is not shown).

of the Ca *K*-edge of spot A indicates that Ca is calcite-like (Fig. 4a), and the spectra of S and P *K*-edges for this spot are very weak [Figs. 4(b) and 4(c)], suggesting that spot A is from crushed sea shells or other Ca-containing remnants of marine organisms with dominating calcium carbonate. For spot B, it appears as a very bright spot because it has high intensity for all three elements. The Ca *K*-edge spectrum is very similar to that of the apatite (Ca-P) (Fig. 4a). In comparison with spot A, the S *K*-edge spectrum of spot B is much more intense (the S *K*-edge spectrum of spot A is acquired with 4 s dwell time, compared with a 1 s dwell time for that of spot B), with the S *K*-edge spectra of both spots composed of contributions from

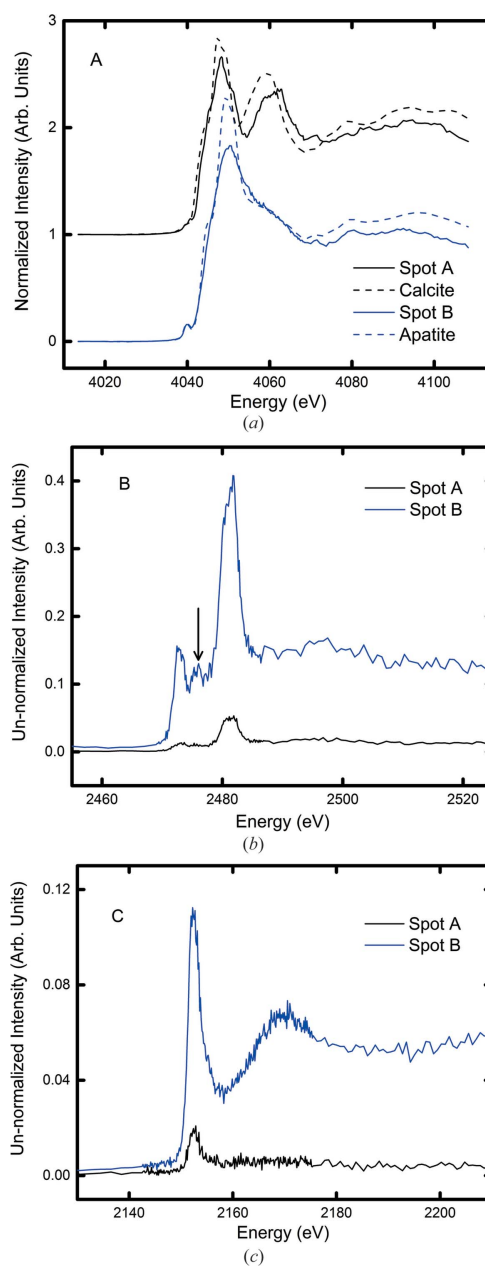


Figure 4

μ -XANES of the Ca *K*-edge (a), S *K*-edge (b) and P *K*-edge (c) of the hot spots A and B, as marked on the tri-colour map in Fig. 3. The un-normalized intensity in (b) and (c) shows the relative concentration of the element.

reduced (peak ~ 2472 eV) and oxidized (peak ~ 2481 eV) sulfur species (Fig. 4b). Additionally, the S *K*-edge spectrum of spot B has another feature around 2475 eV (marked with an arrow, which is absent in the spectrum of spot A), which is normally assigned to the intermediate organic S, further suggesting that spot B has more of an organic origin. Likewise, the P concentration in spot B is much higher [spectra in Figs. 4(b) and 4(c) were acquired under the same conditions and plotted in ‘absolute’ scale for easy comparison of relative concentrations] and a linear combination fitting analysis of the P *K*-edge spectrum for spot B indicates that it has some Ca-, K- and Fe-P compounds (12–15%), but great enrichment with organic phosphates (62%), likely originating from algae or other biological structure, in agreement with the above S *K*-edge result. Thus, μ -XFS and μ -XANES are very powerful in the study of heterogeneously composed biocrusts and these techniques can be used to distinguish between hot spots with different origins containing elevated concentrations of Ca and P.

3.2. Biological applications

Due to the wide range of oxidation states that sulfur exists in within biological systems, a technique with the ability to image both the distribution and the chemical form of S is a highly desired research tool. The potential of XAS to image different chemical forms of S was first described for onion tissue (Pickering *et al.*, 2009) and has since been applied to rodent brain tissue (Szczerbowska-Boruchowska *et al.*, 2012; Hackett *et al.*, 2016a), human prostate tissue (Czapla-Masztafiak *et al.*, 2016), bovine corneal tissue (Veronesi *et al.*, 2013) and fish cartilage tissue (Hackett *et al.*, 2016b). In each of these studies, the ability to detect specific chemical forms of

sulfur, such as thiols, disulfides, sulfonic acids or sulfates, revealed far greater chemical and physiological information than imaging of total sulfur alone. One particular research area expected to benefit greatly from ‘chemically specific’ sulfur imaging is the field of neuroscience. Understanding thiol/disulfide redox and oxidative stress is pertinent to many neurodegenerative diseases or conditions. Micro-XAS at the S *K*-edge has recently been shown capable of studying thiol redox within individual brain cells (Hackett *et al.*, 2015a). Further, taurine, a sulfonic acid, which is abundant in the central nervous system, is implicated in many brain disorders (Hackett *et al.*, 2016b) but cannot be imaged at the cellular level with any technique other than XAS. This is because the XAS features of S in different chemical environments are often distinct. Due to the redox active nature of many forms of sulfur, and the mobile nature of taurine, sample preparation of biological samples is an important consideration for the application of chemically specific sulfur imaging. Recent research on this topic has shown that flash-frozen tissue samples, without chemical fixation, are the most suitable; careful consideration needs to be given if chemically fixed tissue is used (Hackett *et al.*, 2012, 2015b).

The medium-energy microprobe endstation at SXRMB shows great promise for contributing to the field of neuroscience, through chemically specific sulfur imaging (Hackett *et al.*, 2016a,b). An example of the variation in fluorescence intensity that correlates with differential distribution of chemical forms of sulfur, observed for brain tissue excited with different energies across the S *K*-edge, is shown in Fig. 5. The bright field image (Fig. 5a) of the unstrained rat brain tissue section (air-dried unfixed, 20 μ m thick, mounted on a Thermanox plastic coverslip) highlights hippocampal grey matter (red asterisk) and corpus callosum white matter

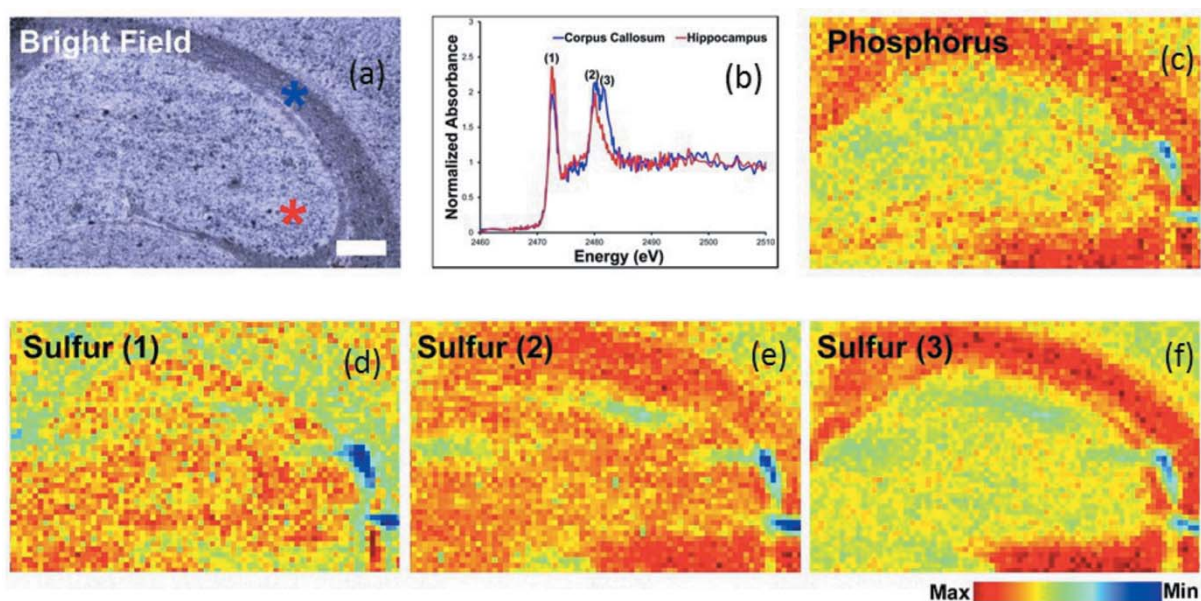


Figure 5 Chemically specific sulfur imaging of brain tissue. Bright field image (a) shows white matter (blue asterisk) and grey matter (red asterisk). (b) Corresponding sulfur micro-XAS spectra are shown in matching colours. Imaging was performed at incident energies of: (c) 2154 eV for phosphorus, (d) 2473.3 eV for low oxidation state sulfur, thiols and disulfides, (e) 2481 eV for sulfonic acids and (f) 2482.6 eV for sulfates. Scale bar = 300 μ m.

(blue asterisk). Micro-XAS spectra (Fig. 5b) collected from these regions highlight a prominent absorption feature (position 1), which is due to low oxidation state sulfur species (thiols and disulfides) present in white matter and grey matter. However, the grey matter contains a stronger absorption edge due to sulfonic acids (position 2) whereas white matter contains a stronger absorption edge due to sulfate esters (position 3). Strong variation in S fluorescence occurs across the tissue sample, when the incident beam energy is set to either position 1, 2 or 3, and reflects differential distribution within white matter and grey matter of low oxidation state sulfur species, sulfonic acids (taurine) and sulfate esters (sulfatide lipids in the myelin sheath), respectively. Such differences have recently been reported, and discussed in detail, for healthy rat brain tissue and brain tissue from rats that have suffered brain ischemia (stroke) (Hackett *et al.*, 2016a).

4. Conclusions

The microprobe endstation at the SXRMB is fully commissioned and ready for general users. We have achieved the beamline performance of a $10\ \mu\text{m} \times 10\ \mu\text{m}$ spot with $\sim 10^9$ photons $(100\ \text{mA})^{-1}\ \text{s}^{-1}$ flux, optimized for the medium-energy range (1.7–5 keV). Chemical mapping and μ -XAFS at P, S and Ca *K*-edges of heterogeneous and low-concentration samples are shown to demonstrate the application of the SXRMB in soil and biological sciences.

Acknowledgements

This work was performed at the Canadian Light Source, which is supported by Natural Science and Engineering Research Council (NSERC) of Canada, National Research Council (NRC) of Canada, the Canadian Institutes of Health Research (CIHR), the Province of Saskatchewan, Western Economic Diversification Canada, and the University of Saskatchewan. The construction of the SXRMB and the microprobe is supported by Canada Foundation for Innovation (CFI), and the Ontario Innovation Trust (OIT). Research at Western is supported by NSERC, CRC, CFI and OIT. We thank the CLS staff for the technical support. MJH was supported by a CIHR Postdoctoral Fellowship, a Saskatchewan Health Research Foundation postdoctoral fellowship, a CIHR training grant in Health Research Using Synchrotron Techniques (CIHR-THRUST) Fellowship, and was a member of the SMI team [Canadian Institutes of Health Research (CIHR)/Heart and Stroke Foundation of Canada (HSFC) Synchrotron Medical Imaging Team Grant #CIF 99472].

References

- Belnap, J. (2011). *Phosphorus in Action, Biological Processes in Soil Phosphorus Cycling*, edited by E. K. Bünemann, A. Oberson and E. Frossard, pp. 371–406. Springer.
- Chadwick, A. V., Berko, A., Schofield, E. J., Jones, A. M., Mosselmans, J. F. W. & Smith, A. D. (2012). *Int. J. Archit. Herit.* **6**, 228–258.
- Czapla-Masztafiak, J., Okon, K., Gałka, M., Huthwelker, T. & Kwiatek, W. M. (2016). *Appl. Spectrosc.* **70**, 264–271.
- Elbert, W., Weber, B., Burrows, S., Steinkamp, J., Büdel, B., Andreae, M. O. & Pöschl, U. (2012). *Nat. Geosci.* **5**, 459–462.
- Hackett, M. J., Britz, C. J., Paterson, P. G., Nichol, H., Pickering, I. J. & George, G. N. (2015b). *ACS Chem. Neurosci.* **6**, 226–238.
- Hackett, M. J., George, G. N., Pickering, I. J. & Eames, B. F. (2016b). *Biochemistry*, **55**, 2441–2451.
- Hackett, M. J., Paterson, P. G., Pickering, I. J. & George, G. N. (2016a). *Anal. Chem.* **88**, 10916–10924.
- Hackett, M. J., Smith, S. E., Caine, S., Nichol, H., George, G. N., Pickering, I. J. & Paterson, P. G. (2015a). *Free Radical Biol. Med.* **89**, 806–818.
- Hackett, M. J., Smith, S. E., Paterson, P. G., Nichol, H., Pickering, I. J. & George, G. N. (2012). *ACS Chem. Neurosci.* **3**, 178–185.
- Heald, S. M., Cross, J. O., Brewster, D. L. & Gordon, R. A. (2007). *Nucl. Instrum. Methods Phys. Res. A*, **582**, 215–217.
- Hitchcock, A. P. (2015). *J. Electron. Spectrosc. Relat. Phenom.* **200**, 49–63.
- Hu, Y. F., Coulthard, I., Chevrier, D., Wright, G., Igarashi, R., Sitnikov, A., Yates, B. W., Hallin, E. L., Sham, T. K., Reiningger, R., Garrett, R., Gentle, I., Nugent, K. & Wilkins, S. (2010). *AIP Conf. Proc.* **1234**, 343–346.
- Igarashi, N., Shimizu, N., Koyama, A., Mori, T., Ohta, H., Niwa, Y., Nitani, H., Abe, H., Nomura, M., Shioya, T., Tsuchiya, K. & Ito, K. (2013). *J. Phys. Conf. Ser.* **425**, 072016.
- Leinweber, P., Baumann, K., Eckhardt, K.-U., Hu, Y., Kruse, J., Michalik, D., Siebers, M., Siebers, N. & Karsten, U. (2017). Submitted.
- Marcus, M. A., MacDowell, A. A., Celestre, R., Manceau, A., Miller, T., Padmore, H. A. & Sublett, R. E. (2004). *J. Synchrotron Rad.* **11**, 239–247.
- Martínez-Criado, G., Tucoulou, R., Cloetens, P., Bleuet, P., Bohic, S., Cauzid, J., Kieffer, I., Kosior, E., Labouré, S., Petitgirard, S., Rack, A., Sans, J. A., Segura-Ruiz, J., Suhonen, H., Susini, J. & Villanova, J. (2012). *J. Synchrotron Rad.* **19**, 10–18.
- Mosselmans, J. F. W., Quinn, P. D., Dent, A. J., Cavill, S. A., Moreno, S. D., Peach, A., Leicester, P. J., Keylock, S. J., Gregory, S. R., Atkinson, K. D. & Rosell, J. R. (2009). *J. Synchrotron Rad.* **16**, 818–824.
- Newville, M., Sutton, S. R., Rivers, M. L. & Eng, P. (1999). *J. Synchrotron Rad.* **6**, 353–355.
- Pickering, I. J., Sneed, E.-Y., Prince, R. C., Block, E., Harris, H. H., Hirsch, G. & George, G. N. (2009). *Biochemistry*, **48**, 6846–6853.
- Szczerbowska-Boruchowska, M., Stegowski, Z., Lankosz, M., Szpak, M. & Adamek, D. (2012). *J. Anal. At. Spectrom.* **27**, 239–247.
- Vantelon, D., Trcera, N., Roy, D., Moreno, T., Mailly, D., Guilet, S., Metchalkov, E., Delmotte, F., Lassalle, B., Lagarde, P. & Flank, A.-M. (2016). *J. Synchrotron Rad.* **23**, 635–640.
- Veronesi, G., Koudouna, E., Cotte, M., Martin, F. L. & Quantock, A. J. (2013). *Anal. Bioanal. Chem.* **405**, 6613–6620.
- West, M., Ellis, A. T., Potts, P. J., Strelly, C., Vanhoof, C. & Wobrauschek, P. (2015). *J. Anal. At. Spectrom.* **30**, 1839–1889.